BELLE2-CONF-PH-2020-011
September 1, 2020

Measurement of Hadronic Mass Moments $\langle M_X^n \rangle$ in $B \to X_c \ell \nu_\ell$ Decays at Belle II

F. Abudinén,[47] I. Adachi,[24,21] R. Adak,[18] K. Adamczyk,[72] P. Ahlburg,[109] J. K. Ahn,[54] H. Aihara,[127] N. Akopov,[133] A. Aloisio,[97,40] F. Ameli,[44] L. Andricek,[63] N. Anh Ky,[37,14] D. M. Asner,[3] H. Atmacan,[111] V. Aulchenko,[4,74] T. Aushev,[26] V. Aushev,[88] T. Aziz,[89] V. Babu,[12] S. Bacher,[72] S. Baehr,[51] S. Bahinipati,[28] A. M. Bakich,[126] P. Bambade,[106] Sw. Banerjee,[116] S. Bansal,[79] M. Barrett,[24] G. Batignani,[100,43] J. Baudot,[107] A. Beaulieu,[129] J. Becker,[51] P. K. Behera,[31] M. Bender,[59] J. V. Bennett,[120] E. Bernieri,[45] F. U. Bernlochner,[109] M. Bertemes,[34] M. Bessner,[113] S. Bettarini,[100,43] V. Bhardwaj,[27] B. Bhuyan,[29] F. Bianchi,[103,46] T. Bilka,[7] S. Bilokin,[59] D. Biswas,[116] A. Bobrov,[4,74] A. Bondar,[4,74] G. Bonvicini,[131] A. Bozek,[72] M. Bračko,[118,87] P. Branchini,[45] N. Braun,[51] R. A. Briere,[5] T. E. Browder,[113] D. N. Brown,[116] A. Budano,[45] L. Burmistrov,[106] S. Bussino,[102,45] M. Campajola,[97,40] L. Cao,[109] G. Caria,[119] G. Casarosa,[100,43] C. Cecchi,[99,42] D. Červenkov,[7] M.-C. Chang,[17] P. Chang,[70] R. Cheaib,[110] V. Chekelian,[62] Y. Q. Chen,[123] Y.-T. Chen,[70] B. G. Cheon,[23] K. Chilikin,[57] K. Chirapatpimol,[8] H.-E. Cho,[23] K. Cho,[53] S.-J. Cho,[134] S.-K. Choi,[22] S. Choudhury,[30] D. Cinabro,[131] L. Corona,[100,43] L. M. Cremaldi,[120] D. Cuesta,[107] S. Cunliffe,[12] T. Czank,[128] N. Dash,[31] F. Dattola,[12] E. De La Cruz-Burelo,[6] G. De Nardo,[97,40] M. De Nuccio,[12] G. De Pietro,[45] R. de Sangro,[39] B. Deschamps,[109] M. Destefanis,[103,46] S. Dey,[91] A. De Yta-Hernandez,[6] A. Di Canto,[3] F. Di Capua,[97,40] S. Di Carlo,[106] J. Dingfelder,[109] Z. Doležal,[7] I. Domínguez Jiménez,[96] T. V. Dong,[18] K. Dort,[50] D. Dossett,[119] S. Dubey,[113] S. Duell,[109] G. Dujany,[107] S. Eidelman,[4,57,74] M. Eliachevitch,[109] D. Epifanov,[4,74] J. E. Fast,[78] T. Ferber,[12] D. Ferlewicz,[119] G. Finocchiaro,[39] S. Fiore,[44] P. Fischer,[114] A. Fodor,[64] F. Forti,[100,43] A. Frey,[19] M. Friedl,[34] B. G. Fulsom,[78] M. Gabriel,[62] N. Gabyshev,[4,74] E. Ganiev,[104,47] M. Garcia-Hernandez,[6] R. Garg,[79] A. Garmash,[4,74] V. Gaur,[130] A. Gaz,[66,67] U. Gebauer,[19] M. Gelb,[51] A. Gellrich,[12] J. Gemmler,[51] T. Geßler,[50] D. Getzkow,[50] R. Giordano,[97,40] A. Giri,[30] A. Glazov,[12] B. Gobbo,[47] R. Godang,[124] P. Goldenzweig,[51] B. Golob,[115,87] P. Gomis,[38] P. Grace,[108] W. Gradl,[49] E. Graziani,[45] D. Greenwald,[90] Y. Guan,[111] C. Hadjivasiliou,[78] S. Halder,[89] K. Hara,[24,21] T. Hara,[24,21] O. Hartbrich,[113] T. Hauth,[51] K. Hayasaka,[73] H. Hayashii,[69] C. Hearty,[110,36] M. Heck,[51] M. T. Hedges,[113] I. Heredia de la Cruz,[6,11] M. Hernández Villanueva,[120] A. Hershenhorn,[110] T. Higuchi,[128] E. C. Hill,[110] H. Hirata,[66] M. Hoek,[49] M. Hohmann,[119] S. Hollitt,[108] T. Hotta,[77] C.-L. Hsu,[126] Y. Hu,[35] K. Huang,[70] T. Iijima,[66,67] K. Inami,[66] G. Inguglia,[34] J. Irakkathil Jabbar,[51] A. Ishikawa,[24,21] R. Itoh,[24,21] M. Iwasaki,[76] Y. Iwasaki,[24] S. Iwata,[95] P. Jackson,[108] W. W. Jacobs,[32] I. Jaegle,[112] D. E. Jaffe,[3] E.-J. Jang,[22] M. Jeandron,[120] H. B. Jeon,[56] S. Jia,[18] Y. Jin,[47] C. Joo,[128] K. K. Joo,[10] I. Kadenko,[88] J. Kahn,[51] H. Kakuno,[95] A. B. Kaliyar,[89] J. Kandra,[7] K. H. Kang,[56] P. Kapusta,[72] R. Karl,[12] G. Karyan,[133] Y. Kato,[66,67] H. Kawai,[9] T. Kawasaki,[52] T. Keck,[51] C. Ketter,[113] H. Kichimi,[24] C. Kiesling,[62] B. H. Kim,[83] C.-H. Kim,[23] D. Y. Kim,[86] H. J. Kim,[56] J. B. Kim,[54] K.-H. Kim,[134] K. Kim,[54] S.-H. Kim,[83]

Y.-K. Kim,[134] Y. Kim,[54] T. D. Kimmel,[130] H. Kindo,[24,21] K. Kinoshita,[111] B. Kirby,[3] C. Kleinwort,[12] B. Knysh,[106] P. Kodyš,[7] T. Koga,[24] S. Kohani,[113] I. Komarov,[12] T. Konno,[52] S. Korpar,[118,87] N. Kovalchuk,[12] T. M. G. Kraetzschmar,[62] P. Križan,[115,87] R. Kroeger,[120] J. F. Krohn,[119] P. Krokovny,[4,74] H. Krüger,[109] W. Kuehn,[50] T. Kuhr,[59] J. Kumar,[5] M. Kumar,[61] R. Kumar,[81] K. Kumara,[131] T. Kumita,[95] T. Kunigo,[24] M. Künzel,[12,59] S. Kurz,[12] A. Kuzmin,[4,74] P. Kvasnička,[7] Y.-J. Kwon,[134] S. Lacaprara,[41] Y.-T. Lai,[128] C. La Licata,[128] K. Lalwani,[61] L. Lanceri,[47] J. S. Lange,[50] K. Lautenbach,[50] P. J. Laycock,[3] F. R. Le Diberder,[106] I.-S. Lee,[23] S. C. Lee,[56] P. Leitl,[62] D. Levit,[90] P. M. Lewis,[109] C. Li,[58] L. K. Li,[111] S. X. Li,[2] Y. M. Li,[35] Y. B. Li,[80] J. Libby,[31] K. Lieret,[59] L. Li Gioi,[62] J. Lin,[70] Z. Liptak,[113] Q. Y. Liu,[12] Z. A. Liu,[35] D. Liventsev,[131,24] S. Longo,[12] A. Loos,[125] P. Lu,[70] M. Lubej,[87] T. Lueck,[59] F. Luetticke,[109] T. Luo,[18] C. MacQueen,[119] Y. Maeda,[66,67] M. Maggiora,[103,46] S. Maity,[28] R. Manfredi,[104,47] E. Manoni,[42] S. Marcello,[103,46] C. Marinas,[38] A. Martini,[102,45] M. Masuda,[15,77] T. Matsuda,[121] K. Matsuoka,[66,67] D. Matvienko,[4,57,74] J. McNeil,[112] F. Meggendorfer,[62] J. C. Mei,[18] F. Meier,[13] M. Merola,[97,40] F. Metzner,[51] M. Milesi,[119] C. Miller,[129] K. Miyabayashi,[69] H. Miyake,[24,21] H. Miyata,[73] R. Mizuk,[57,26] K. Azmi,[117] G. B. Mohanty,[89] H. Moon,[54] T. Moon,[83] J. A. Mora Grimaldo,[127] A. Morda,[41] T. Morii,[128] H.-G. Moser,[62] M. Mrvar,[34] F. Mueller,[62] F. J. Müller,[12] Th. Muller,[51] G. Muroyama,[66] C. Murphy,[128] R. Mussa,[46] K. Nakagiri,[24] I. Nakamura,[24,21] K. R. Nakamura,[24,21] E. Nakano,[76] M. Nakao,[24,21] H. Nakayama,[24,21] H. Nakazawa,[70] T. Nanut,[87] Z. Natkaniec,[72] A. Natochii,[113] M. Nayak,[91] G. Nazaryan,[133] D. Neverov,[66] C. Niebuhr,[12] M. Niiyama,[55] J. Ninkovic,[63] N. K. Nisar,[3] S. Nishida,[24,21] K. Nishimura,[113] M. Nishimura,[24] M. H. A. Nouxman,[117] B. Oberhof,[39] K. Ogawa,[73] S. Ogawa,[92] S. L. Olsen,[22] Y. Onishchuk,[88] H. Ono,[73] Y. Onuki,[127] P. Oskin,[57] E. R. Oxford,[5] H. Ozaki,[24,21] P. Pakhlov,[57,65] G. Pakhlova,[26,57] A. Paladino,[100,43] T. Pang,[122] A. Panta,[120] E. Paoloni,[100,43] S. Pardi,[40] C. Park,[134] H. Park,[56] S.-H. Park,[134] B. Paschen,[109] A. Passeri,[45] A. Pathak,[116] S. Patra,[27] S. Paul,[90] T. K. Pedlar,[60] I. Peruzzi,[39] R. Peschke,[113] R. Pestotnik,[87] M. Piccolo,[39] L. E. Piilonen,[130] P. L. M. Podesta-Lerma,[96] G. Polat,[1] V. Popov,[26] C. Praz,[12] E. Prencipe,[16] M. T. Prim,[109] M. V. Purohit,[75] N. Rad,[12] P. Rados,[12] R. Rasheed,[107] M. Reif,[62] S. Reiter,[50] M. Remnev,[4,74] P. K. Resmi,[31] I. Ripp-Baudot,[107] M. Ritter,[59] M. Ritzert,[114] G. Rizzo,[100,43] L. B. Rizzuto,[87] S. H. Robertson,[64,36] D. Rodríguez Pérez,[96] J. M. Roney,[129,36] C. Rosenfeld,[125] A. Rostomyan,[12] N. Rout,[31] M. Rozanska,[72] G. Russo,[97,40] D. Sahoo,[89] Y. Sakai,[24,21] D. A. Sanders,[120] S. Sandilya,[111] A. Sangal,[111] L. Santelj,[115,87] P. Sartori,[98,41] J. Sasaki,[127] Y. Sato,[93] V. Savinov,[122] B. Scavino,[49] M. Schram,[78] H. Schreeck,[19] J. Schueler,[113] C. Schwanda,[34] A. J. Schwartz,[111] B. Schwenker,[19] R. M. Seddon,[64] Y. Seino,[73] A. Selce,[101,44] K. Senyo,[132] I. S. Seong,[113] J. Serrano,[1] M. E. Sevior,[119] C. Sfienti,[49] V. Shebalin,[113] C. P. Shen,[2] H. Shibuya,[92] J.-G. Shiu,[70] B. Shwartz,[4,74] A. Sibidanov,[129] F. Simon,[62] J. B. Singh,[79] S. Skambraks,[62] K. Smith,[119] R. J. Sobie,[129,36] A. Soffer,[91] A. Sokolov,[33] Y. Soloviev,[12] E. Solovieva,[57] S. Spataro,[103,46] B. Spruck,[49] M. Starič,[87] S. Stefkova,[12] Z. S. Stottler,[130] R. Stroili,[98,41] J. Strube,[78] J. Stypula,[72] M. Sumihama,[20,77] K. Sumisawa,[24,21] T. Sumiyoshi,[95] D. J. Summers,[120] W. Sutcliffe,[109] K. Suzuki,[66] S. Y. Suzuki,[24,21] H. Svidras,[12] M. Tabata,[9] M. Takahashi,[12] M. Takizawa,[82,25,84] U. Tamponi,[46] S. Tanaka,[24,21] K. Tanida,[48] H. Tanigawa,[127] N. Taniguchi,[24] Y. Tao,[112] P. Taras,[105] F. Tenchini,[12] D. Tonelli,[47] E. Torassa,[41] K. Trabelsi,[106] T. Tsuboyama,[24,21] N. Tsuzuki,[66] M. Uchida,[94] I. Ueda,[24,21] S. Uehara,[24,21] T. Ueno,[93] T. Uglov,[57,26] K. Unger,[51] Y. Unno,[23] S. Uno,[24,21] P. Urquijo,[119] Y. Ushiroda,[24,21,127] Y. Usov,[4,74] S. E. Vahsen,[113] R. van Tonder,[109] G. S. Varner,[113] K. E. Varvell,[126] A. Vinokurova,[4,74] L. Vitale,[104,47] V. Vorobyev,[4,57,74] A. Vossen,[13] E. Waheed,[24]

H. M. Wakeling,[64] K. Wan,[127] W. Wan Abdullah,[117] B. Wang,[62] C. H. Wang,[71] M.-Z. Wang,[70] X. L. Wang,[18] A. Warburton,[64] M. Watanabe,[73] S. Watanuki,[106] I. Watson,[127] J. Webb,[119] S. Wehle,[12] M. Welsch,[109] C. Wessel,[109] J. Wiechczynski,[43] P. Wieduwilt,[19] H. Windel,[62] E. Won,[54] L. J. Wu,[35] X. P. Xu,[85] B. Yabsley,[126] S. Yamada,[24] W. Yan,[123] S. B. Yang,[54] H. Ye,[12] J. Yelton,[112] I. Yeo,[53] J. H. Yin,[54] M. Yonenaga,[95] Y. M. Yook,[35] T. Yoshinobu,[73] C. Z. Yuan,[35] G. Yuan,[123] W. Yuan,[41] Y. Yusa,[73] L. Zani,[1] J. Z. Zhang,[35] Y. Zhang,[123] Z. Zhang,[123] V. Zhilich,[4,74] Q. D. Zhou,[66,68] X. Y. Zhou,[2] V. I. Zhukova,[57] V. Zhulanov,[4,74] and A. Zupanc[87]

(Belle II Collaboration)

[1]*Aix Marseille Université, CNRS/IN2P3, CPPM, 13288 Marseille, France*
[2]*Beihang University, Beijing 100191, China*
[3]*Brookhaven National Laboratory, Upton, New York 11973, U.S.A.*
[4]*Budker Institute of Nuclear Physics SB RAS, Novosibirsk 630090, Russian Federation*
[5]*Carnegie Mellon University, Pittsburgh, Pennsylvania 15213, U.S.A.*
[6]*Centro de Investigacion y de Estudios Avanzados del Instituto Politecnico Nacional, Mexico City 07360, Mexico*
[7]*Faculty of Mathematics and Physics, Charles University, 121 16 Prague, Czech Republic*
[8]*Chiang Mai University, Chiang Mai 50202, Thailand*
[9]*Chiba University, Chiba 263-8522, Japan*
[10]*Chonnam National University, Gwangju 61186, South Korea*
[11]*Consejo Nacional de Ciencia y Tecnología, Mexico City 03940, Mexico*
[12]*Deutsches Elektronen–Synchrotron, 22607 Hamburg, Germany*
[13]*Duke University, Durham, North Carolina 27708, U.S.A.*
[14]*Institute of Theoretical and Applied Research (ITAR), Duy Tan University, Hanoi 100000, Vietnam*
[15]*Earthquake Research Institute, University of Tokyo, Tokyo 113-0032, Japan*
[16]*Forschungszentrum Jülich, 52425 Jülich, Germany*
[17]*Department of Physics, Fu Jen Catholic University, Taipei 24205, Taiwan*
[18]*Key Laboratory of Nuclear Physics and Ion-beam Application (MOE) and Institute of Modern Physics, Fudan University, Shanghai 200443, China*
[19]*II. Physikalisches Institut, Georg-August-Universität Göttingen, 37073 Göttingen, Germany*
[20]*Gifu University, Gifu 501-1193, Japan*
[21]*The Graduate University for Advanced Studies (SOKENDAI), Hayama 240-0193, Japan*
[22]*Gyeongsang National University, Jinju 52828, South Korea*
[23]*Department of Physics and Institute of Natural Sciences, Hanyang University, Seoul 04763, South Korea*
[24]*High Energy Accelerator Research Organization (KEK), Tsukuba 305-0801, Japan*
[25]*J-PARC Branch, KEK Theory Center, High Energy Accelerator Research Organization (KEK), Tsukuba 305-0801, Japan*
[26]*Higher School of Economics (HSE), Moscow 101000, Russian Federation*
[27]*Indian Institute of Science Education and Research Mohali, SAS Nagar, 140306, India*
[28]*Indian Institute of Technology Bhubaneswar, Satya Nagar 751007, India*
[29]*Indian Institute of Technology Guwahati, Assam 781039, India*
[30]*Indian Institute of Technology Hyderabad, Telangana 502285, India*
[31]*Indian Institute of Technology Madras, Chennai 600036, India*
[32]*Indiana University, Bloomington, Indiana 47408, U.S.A.*
[33]*Institute for High Energy Physics, Protvino 142281, Russian Federation*
[34]*Institute of High Energy Physics, Vienna 1050, Austria*

[35]*Institute of High Energy Physics, Chinese Academy of Sciences, Beijing 100049, China*
[36]*Institute of Particle Physics (Canada), Victoria, British Columbia V8W 2Y2, Canada*
[37]*Institute of Physics, Vietnam Academy of Science and Technology (VAST), Hanoi, Vietnam*
[38]*Instituto de Fisica Corpuscular, Paterna 46980, Spain*
[39]*INFN Laboratori Nazionali di Frascati, I-00044 Frascati, Italy*
[40]*INFN Sezione di Napoli, I-80126 Napoli, Italy*
[41]*INFN Sezione di Padova, I-35131 Padova, Italy*
[42]*INFN Sezione di Perugia, I-06123 Perugia, Italy*
[43]*INFN Sezione di Pisa, I-56127 Pisa, Italy*
[44]*INFN Sezione di Roma, I-00185 Roma, Italy*
[45]*INFN Sezione di Roma Tre, I-00146 Roma, Italy*
[46]*INFN Sezione di Torino, I-10125 Torino, Italy*
[47]*INFN Sezione di Trieste, I-34127 Trieste, Italy*
[48]*Advanced Science Research Center, Japan Atomic Energy Agency, Naka 319-1195, Japan*
[49]*Johannes Gutenberg-Universität Mainz, Institut für Kernphysik, D-55099 Mainz, Germany*
[50]*Justus-Liebig-Universität Gießen, 35392 Gießen, Germany*
[51]*Institut für Experimentelle Teilchenphysik, Karlsruher Institut für Technologie, 76131 Karlsruhe, Germany*
[52]*Kitasato University, Sagamihara 252-0373, Japan*
[53]*Korea Institute of Science and Technology Information, Daejeon 34141, South Korea*
[54]*Korea University, Seoul 02841, South Korea*
[55]*Kyoto Sangyo University, Kyoto 603-8555, Japan*
[56]*Kyungpook National University, Daegu 41566, South Korea*
[57]*P.N. Lebedev Physical Institute of the Russian Academy of Sciences, Moscow 119991, Russian Federation*
[58]*Liaoning Normal University, Dalian 116029, China*
[59]*Ludwig Maximilians University, 80539 Munich, Germany*
[60]*Luther College, Decorah, Iowa 52101, U.S.A.*
[61]*Malaviya National Institute of Technology Jaipur, Jaipur 302017, India*
[62]*Max-Planck-Institut für Physik, 80805 München, Germany*
[63]*Semiconductor Laboratory of the Max Planck Society, 81739 München, Germany*
[64]*McGill University, Montréal, Québec, H3A 2T8, Canada*
[65]*Moscow Physical Engineering Institute, Moscow 115409, Russian Federation*
[66]*Graduate School of Science, Nagoya University, Nagoya 464-8602, Japan*
[67]*Kobayashi-Maskawa Institute, Nagoya University, Nagoya 464-8602, Japan*
[68]*Institute for Advanced Research, Nagoya University, Nagoya 464-8602, Japan*
[69]*Nara Women's University, Nara 630-8506, Japan*
[70]*Department of Physics, National Taiwan University, Taipei 10617, Taiwan*
[71]*National United University, Miao Li 36003, Taiwan*
[72]*H. Niewodniczanski Institute of Nuclear Physics, Krakow 31-342, Poland*
[73]*Niigata University, Niigata 950-2181, Japan*
[74]*Novosibirsk State University, Novosibirsk 630090, Russian Federation*
[75]*Okinawa Institute of Science and Technology, Okinawa 904-0495, Japan*
[76]*Osaka City University, Osaka 558-8585, Japan*
[77]*Research Center for Nuclear Physics, Osaka University, Osaka 567-0047, Japan*
[78]*Pacific Northwest National Laboratory, Richland, Washington 99352, U.S.A.*
[79]*Panjab University, Chandigarh 160014, India*
[80]*Peking University, Beijing 100871, China*
[81]*Punjab Agricultural University, Ludhiana 141004, India*

[82]Meson Science Laboratory, Cluster for Pioneering Research, RIKEN, Saitama 351-0198, Japan
[83]Seoul National University, Seoul 08826, South Korea
[84]Showa Pharmaceutical University, Tokyo 194-8543, Japan
[85]Soochow University, Suzhou 215006, China
[86]Soongsil University, Seoul 06978, South Korea
[87]J. Stefan Institute, 1000 Ljubljana, Slovenia
[88]Taras Shevchenko National Univ. of Kiev, Kiev, Ukraine
[89]Tata Institute of Fundamental Research, Mumbai 400005, India
[90]Department of Physics, Technische Universität München, 85748 Garching, Germany
[91]Tel Aviv University, School of Physics and Astronomy, Tel Aviv, 69978, Israel
[92]Toho University, Funabashi 274-8510, Japan
[93]Department of Physics, Tohoku University, Sendai 980-8578, Japan
[94]Tokyo Institute of Technology, Tokyo 152-8550, Japan
[95]Tokyo Metropolitan University, Tokyo 192-0397, Japan
[96]Universidad Autonoma de Sinaloa, Sinaloa 80000, Mexico
[97]Dipartimento di Scienze Fisiche, Università di Napoli Federico II, I-80126 Napoli, Italy
[98]Dipartimento di Fisica e Astronomia, Università di Padova, I-35131 Padova, Italy
[99]Dipartimento di Fisica, Università di Perugia, I-06123 Perugia, Italy
[100]Dipartimento di Fisica, Università di Pisa, I-56127 Pisa, Italy
[101]Università di Roma "La Sapienza," I-00185 Roma, Italy
[102]Dipartimento di Matematica e Fisica, Università di Roma Tre, I-00146 Roma, Italy
[103]Dipartimento di Fisica, Università di Torino, I-10125 Torino, Italy
[104]Dipartimento di Fisica, Università di Trieste, I-34127 Trieste, Italy
[105]Université de Montréal, Physique des Particules, Montréal, Québec, H3C 3J7, Canada
[106]Université Paris-Saclay, CNRS/IN2P3, IJCLab, 91405 Orsay, France
[107]Université de Strasbourg, CNRS, IPHC, UMR 7178, 67037 Strasbourg, France
[108]Department of Physics, University of Adelaide, Adelaide, South Australia 5005, Australia
[109]University of Bonn, 53115 Bonn, Germany
[110]University of British Columbia, Vancouver, British Columbia, V6T 1Z1, Canada
[111]University of Cincinnati, Cincinnati, Ohio 45221, U.S.A.
[112]University of Florida, Gainesville, Florida 32611, U.S.A.
[113]University of Hawaii, Honolulu, Hawaii 96822, U.S.A.
[114]University of Heidelberg, 68131 Mannheim, Germany
[115]Faculty of Mathematics and Physics, University of Ljubljana, 1000 Ljubljana, Slovenia
[116]University of Louisville, Louisville, Kentucky 40292, U.S.A.
[117]National Centre for Particle Physics, University Malaya, 50603 Kuala Lumpur, Malaysia
[118]University of Maribor, 2000 Maribor, Slovenia
[119]School of Physics, University of Melbourne, Victoria 3010, Australia
[120]University of Mississippi, University, Mississippi 38677, U.S.A.
[121]University of Miyazaki, Miyazaki 889-2192, Japan
[122]University of Pittsburgh, Pittsburgh, Pennsylvania 15260, U.S.A.
[123]University of Science and Technology of China, Hefei 230026, China
[124]University of South Alabama, Mobile, Alabama 36688, U.S.A.
[125]University of South Carolina, Columbia, South Carolina 29208, U.S.A.
[126]School of Physics, University of Sydney, New South Wales 2006, Australia
[127]Department of Physics, University of Tokyo, Tokyo 113-0033, Japan
[128]Kavli Institute for the Physics and Mathematics of the Universe (WPI), University of Tokyo, Kashiwa 277-8583, Japan
[129]University of Victoria, Victoria, British Columbia, V8W 3P6, Canada

[130] *Virginia Polytechnic Institute and State University, Blacksburg, Virginia 24061, U.S.A.*
[131] *Wayne State University, Detroit, Michigan 48202, U.S.A.*
[132] *Yamagata University, Yamagata 990-8560, Japan*
[133] *Alikhanyan National Science Laboratory, Yerevan 0036, Armenia*
[134] *Yonsei University, Seoul 03722, South Korea*

Abstract

We present measurements of the first six hadronic mass moments in semileptonic $B \to X_c \ell \nu_\ell$ decays. The hadronic mass moments, together with other observables of inclusive B decays, can be used to determine the CKM matrix element $|V_{cb}|$ and mass of the b-quark m_b in the context of Heavy Quark Expansions of QCD. The Belle II data recorded at the $\Upsilon(4S)$ resonance in 2019 and 2020 (March-July), corresponding to an integrated luminosity of $34.6\,\mathrm{fb}^{-1}$, is used for this measurement. The decay $\Upsilon(4S) \to B\overline{B}$ is reconstructed by applying the hadronic tagging algorithm provided by the Full Event Interpretation to fully reconstruct one B meson. The second B meson is reconstructed inclusively by selecting a high-momentum lepton. The X_c system is identified by the remaining reconstructed tracks and clusters in the electromagnetic calorimeter. We report preliminary results for the hadronic mass moments $\langle M_X^n \rangle$ with $n = 1, \ldots, 6$, measured as a function of a lower cut on the lepton momentum in the signal B rest frame.

1. INTRODUCTION

The mass moments $\langle M_X^n \rangle$ of the hadronic system in inclusive semileptonic $B \to X_c \ell \nu_\ell$ decays can be used to measure non-perturbative QCD parameters and the CKM matrix element $|V_{cb}|$. The state-of-the-art procedure relies on combining the information from mass moments, with measured moments from the lepton energy spectrum and $B \to X_s \gamma$ information, to perform a combined fit using theory predictions building on the Heavy Quark Expansions of QCD to determine $|V_{cb}|$ and the b quark mass m_b, see e.g. [1] for a recent review.

This work presents the first results of hadronic mass moments $\langle M_X^n \rangle$ with $n = 1, \ldots, 6$, measured at the Belle II experiment. In this analysis, semileptonic $B \to X_c \ell \nu_\ell$ decays are reconstructed inclusively by selecting a high-momentum lepton. The other B meson is fully reconstructed in hadronic modes via the Full Event Interpretation (FEI) [2]. This B meson is referred to as the tag-side B meson (B_{tag}) throughout this note. We subtract the remaining background components by assigning a continuous signal probability as a function of the reconstructed mass of the hadronic X_c system (M_X) to each event. A calibration procedure is applied to correct for a bias in the reconstructed M_X spectrum due to experimental effects. The hadronic mass moments are calculated as a weighted mean of the calibrated M_X distribution, where the events are weighted with the aforementioned signal probability.

The rest of this note is organized as follows. Section 2 briefly describes the Belle II detector and how the inclusive $B \to X_c \ell \nu_\ell$ decays are simulated. The reconstruction of the $\Upsilon(4S)$ event is discussed in Section 3. The procedure for subtracting remaining background components from the measured M_X spectrum is introduced in Section 4. Section 5 discusses the extraction and calibration of the reconstructed M_X distributions. In addition, the handling of statistical and systematic uncertainties is explained and the measured M_X values are given. Finally, Section 6 presents our conclusions.

2. BELLE II DETECTOR AND DATA SET

The Belle II detector [3] is operated at the SuperKEKB electron-positron collider [4] and is located at the KEK laboratory in Tsukuba, Japan. The detector consists of several nested detector subsystems arranged around the beam pipe in a cylindrical geometry. Sub-detectors relevant for this analysis are briefly described here; a description of the full detector is given in [3, 5]. The innermost subsystem is the vertex detector, which includes two layers of silicon pixel detectors and four outer layers of silicon strip detectors. Currently, the second pixel layer is installed to cover only a small part of the solid angle, while the remaining vertex detector layers are fully installed. Most of the tracking volume consists of a helium and ethane-based small-cell drift chamber. Surrounding the drift chamber (CDC), the Cherenkov-light imaging and time-of-propagation detector provides charged-particle identification in the barrel region. In the forward end-cap, this function is provided by a proximity-focusing, ring-imaging Cherenkov detector with aerogel radiator. The next sub-detector layer consists of the electromagnetic calorimeter (ECL), composed of barrel and two end-cap sections made of CsI(Tl) crystals. The inner detector is immersed in a uniform magnetic field with a field strength of 1.5 T from the superconducting solenoid situated outside the calorimeter. Multiple layers of scintillators and resistive plate chambers, located between the magnetic flux-return iron plates, constitute the K_L^0 and muon identification system.

The data sample used in this analysis was collected in 2019 and from March to July 2020 at a center-of-mass (CM) energy of $\sqrt{s} = 10.58\,\text{GeV}$, corresponding to the mass of the $\Upsilon(4S)$ resonance. The energies of the electron and positron beams are 7 GeV and 4 GeV, respectively, resulting in a boost of $\beta\gamma = 0.28$ of the CM frame relative to the laboratory frame. The integrated luminosity of

TABLE I: Branching fractions used in the simulation of $B \to X_c \ell \nu_\ell$ decays in this analysis

$\mathcal{B}$	Value B^+	Value B^0
$B \to D\,\ell^+\,\nu_\ell$	$(2.3 \pm 0.1) \times 10^{-2}$	$(2.1 \pm 0.1) \times 10^{-2}$
$B \to D^*\,\ell^+\,\nu_\ell$	$(5.5 \pm 0.1) \times 10^{-2}$	$(5.1 \pm 0.1) \times 10^{-2}$
$B \to D_1\,\ell^+\,\nu_\ell$	$(4.5 \pm 0.3) \times 10^{-3}$	$(4.2 \pm 0.3) \times 10^{-3}$
$(\hookrightarrow D^*\pi)$		
$B \to D_1\,\ell^+\,\nu_\ell$	$(3.2 \pm 1.0) \times 10^{-3}$	$(2.8 \pm 0.9) \times 10^{-3}$
$(\hookrightarrow D\pi\pi)$		
$B \to D_2^*\,\ell^+\,\nu_\ell$	$(1.5 \pm 0.1) \times 10^{-3}$	$(1.4 \pm 0.1) \times 10^{-3}$
$(\hookrightarrow D^*\pi)$		
$B \to D_2^*\,\ell^+\,\nu_\ell$	$(2.2 \pm 0.2) \times 10^{-3}$	$(2.1 \pm 0.2) \times 10^{-3}$
$(\hookrightarrow D\pi)$		
$B \to D_0^*\,\ell^+\,\nu_\ell$	$(3.9 \pm 0.8) \times 10^{-3}$	$(3.6 \pm 0.7) \times 10^{-3}$
$(\hookrightarrow D\pi)$		
$B \to D_1'\,\ell^+\,\nu_\ell$	$(4.3 \pm 0.8) \times 10^{-3}$	$(4.0 \pm 0.8) \times 10^{-3}$
$(\hookrightarrow D^*\pi)$		
$B \to D\pi\,\ell^+\,\nu_\ell$	$(1.5 \pm 0.6) \times 10^{-3}$	$(1.5 \pm 0.6) \times 10^{-3}$
$B \to D^*\pi\,\ell^+\,\nu_\ell$	$(1.5 \pm 1.0) \times 10^{-3}$	$(1.5 \pm 1.0) \times 10^{-3}$
$B \to D\pi\pi\,\ell^+\,\nu_\ell$	$(0.5 \pm 0.5) \times 10^{-3}$	$(0.5 \pm 0.5) \times 10^{-3}$
$B \to D^*\pi\pi\,\ell^+\,\nu_\ell$	$(2.6 \pm 1.0) \times 10^{-3}$	$(2.4 \pm 1.0) \times 10^{-3}$
$B \to D\eta\,\ell^+\,\nu_\ell$	$(2.0 \pm 2.0) \times 10^{-3}$	$(2.2 \pm 2.2) \times 10^{-3}$
$B \to D^*\eta\,\ell^+\,\nu_\ell$	$(2.0 \pm 2.0) \times 10^{-3}$	$(2.2 \pm 2.2) \times 10^{-3}$
$B \to X_c \ell \nu_\ell$	$(10.8 \pm 0.4) \times 10^{-2}$	$(10.0 \pm 0.4) \times 10^{-2}$

the data sample amounts to $34.6\,\text{fb}^{-1}$.

Monte Carlo (MC) samples of B meson decays are simulated using the `EvtGen` generator [6]. The sample size corresponds to an integrated luminosity of $200\,\text{fb}^{-1}$. The interactions of particles inside the detector are simulated using `Geant4` [7]. Electromagnetic final-state radiation (FSR) is simulated using the `PHOTOS` [8] package. The simulation of the continuum background process $e^+e^- \to q\bar{q}$ ($q = u, d, s, c$) is carried out with `KKMC` [9], interfaced with `Pythia` [10]. All recorded collisions and simulated events were analyzed in the basf2 [11] framework and a summary of the track reconstruction algorithms can be found in Ref. [12].

The $B \to X_c \ell \nu_\ell$ spectrum is modeled as a mixture of resonant and non-resonant decays. $B \to D \ell \nu_\ell$ decays are modeled using the BGL form factors [13] with central values taken from the fit in Ref. [14]. To simulate $B \to D^* \ell \nu_\ell$ decays, the CLN form factors [15] are used with central values taken from Ref. [16]. The decays of the four orbitally excited D meson states (D_1, D_2^*, D_1' and D_0^*), denoted as D^{**}, are simulated with a LLSW form factor inspired parametrization [17], using the central values and parametrization from Ref. [18]. The non-resonant part of the X_c spectrum is simulated as a composition of $B \to D^{(*)}\pi\ell\nu_\ell$, $B \to D^{(*)}\pi\pi\ell\nu_\ell$ and $B \to D^{(*)}\eta\ell\nu_\ell$ decays. The first decay is simulated using the decay model proposed by Goity and Roberts [19], while the remaining two decays are modeled with a pure phase-space prescription. The branching fractions used for the simulation of $B \to X_c \ell \nu_\ell$ decays are given in Table I.

3. EVENT RECONSTRUCTION

$\Upsilon(4S) \to B\overline{B}$ events are tagged by fully reconstructing one B meson decaying hadronically, also

referred to as the tag-side B_{tag} meson. The other B meson is reconstructed inclusively by selecting a high-momentum lepton. The X-system is defined by the rest of the event (ROE), consisting of additional unassigned charged particles and neutral clusters in the ECL. Event-level pre-cuts are applied to reduce the number of continuum and low-multiplicity background components. We select events with at least four reconstructed charged tracks. Additionally, we require at least two tracks with $|d_0| < 0.5\,\text{cm}$, $|z_0| < 2\,\text{cm}$ and $p_T > 0.1\,\text{GeV}/c$, as well as at least two ECL clusters with $E > 0.1\,\text{GeV}$ and a polar angle θ inside the CDC acceptance. Here, z_0 denotes the signed distance to the z direction (parallel to the beams and the magnetic field) of closest approach to the interaction point (POCA). Further, d_0 is the signed distance transverse to the z direction to the POCA. To reject continuum events, the event is required to pass $R_2 < 0.4$, where R_2 is the ratio of the second to the zeroth Fox-Wolfram moment [20]. These event shape variables are calculated using all charged tracks and ECL clusters passing the selection criteria mentioned above. Finally, the event is required to have a greater visible energy in the CM frame than 4 GeV, while the total energy in the ECL is required to lie between $2 < E_{\text{ECL}} < 7\,\text{GeV}$.

3.1. Hadronic Tag-Side Reconstruction

The tag-side B_{tag} candidate is reconstructed using the hadronic tagging algorithm provided by the Full Event Interpretation (FEI) [2]. The FEI uses a fully automated approach to hierarchically reconstruct a tag-side B meson and infers a signal probability $\mathcal{P}_{\text{FEI}}$ for each reconstructed B_{tag} candidate based on multivariate analysis (MVA) techniques. The algorithm uses an exclusive reconstruction approach resulting in $\mathcal{O}(10'000)$ distinct B decay chains. We use a skimmed version of the data with reconstructed B_{tag} candidates passing $\mathcal{P}_{\text{FEI}} > 0.001$, $M_{\text{bc}} > 5.24\,\text{GeV}/c^2$ and $|\Delta E| < 0.2\,\text{GeV}$. The beam-constrained mass M_{bc} and energy difference ΔE are defined as

$$M_{\text{bc}} = \sqrt{\frac{s}{4} - (\mathbf{p}^*_{B_{\text{tag}}})^2}, \tag{1}$$

$$\Delta E = E^*_{B_{\text{tag}}} - \frac{\sqrt{s}}{2}, \tag{2}$$

where $\mathbf{p}^*_{B_{\text{tag}}}$ and $E^*_{B_{\text{tag}}}$ denote the reconstructed B_{tag} three-momentum and energy, respectively, in the CM frame. To further reduce the combinatorial complexity, only the three candidates with the highest FEI signal probability per event for the B_{tag} candidates are considered in the subsequent stages of the analysis.

3.2. Selection of Inclusive $B \to X\ell\nu_\ell$ Decays

We select $e^\pm$, $\mu^\pm$ and $K^\pm$ candidates by using the normalized charged particle identification (PID) from sub-detector information. The $e^\pm$, $\mu^\pm$ and $K^\pm$ candidates are required to have a PID value greater than 0.9, 0.9 and 0.6, respectively. Additionally, the respective tracks are required to pass $dr < 1\,\text{cm}$, $|dz| < 2\,\text{cm}$, have at least one hit in the CDC and a θ value inside the CDC acceptance. Here, dr and dz denote the track's d_0 and z_0 values, respectively, of its POCA relative to the interaction point. To construct the ROE object, we reconstruct all remaining tracks and ECL clusters assuming that they are $\pi^\pm$ and photons, respectively.

Electron candidates are corrected for bremsstrahlung by identifying suitable photon candidates. At this stage, the selected light-lepton candidates ($\ell = e, \mu$) are combined with the B_{tag} candidates to form an $\Upsilon(4S)$ candidate. Due to the fully reconstructed tag-side candidate and the known initial state of the e^+e^- collision, the lepton momentum in the signal B rest frame, denoted as p^*_ℓ,

is accessible. We require lepton candidates with $p^*_\ell > 0.6\,\mathrm{GeV}/c$. The charge correlations between the b quark of the B_{tag} and the signal lepton candidates are not considered when recombining the $\Upsilon(4S)$ candidate, resulting in the eight reconstruction channels $B^+_{\mathrm{tag}}\ell^\pm$ and $B^0_{\mathrm{tag}}\ell^\pm$. In the final analysis, only the $B^+_{\mathrm{tag}}\ell^-$ and $B^0_{\mathrm{tag}}\ell^\pm$ are considered as signal channels. The two $B^+_{\mathrm{tag}}\ell^+$ channels are background enriched and used to verify the description of the background modeling.

The hadronic X-system is identified from the ROE of the $\Upsilon(4S)$ candidate. The ROE is constructed using the remaining charged particle and photon candidates that were not used in the reconstruction of the $\Upsilon(4S)$ candidate. The mass hypothesis of the individual track object is based on the PID selection. Remaining tracks associated with a kaon likelihood greater than 0.6 are assigned the kaon mass, while all other ROE tracks are identified as pions. To remove background candidates that do not belong to the $\Upsilon(4S)$ decay, we consider only tracks in the ROE with $dr < 2\,\mathrm{cm}$, $|dz| < 4\,\mathrm{cm}$, at least one hit in the CDC and a θ value within the CDC acceptance. Low-momentum tracks curling inside the CDC are removed prior to construction of the ROE. Photon candidates are required to pass a region-dependent cut. We select only photons with $p_T > 20\,\mathrm{MeV}$ and $\mathcal{P}_{\mathrm{Zernike}} > 0.35$, $p_T > 30\,\mathrm{MeV}$ and $\mathcal{P}_{\mathrm{Zernike}} > 0.15$ and $p_T > 20\,\mathrm{MeV}$ and $\mathcal{P}_{\mathrm{Zernike}} > 0.4$ for the forward end-cap, barrel, and backward end-cap ECL region, respectively. $\mathcal{P}_{\mathrm{Zernike}}$ denotes the MVA classifier output using Zernike moments of the different clusters. A second ROE object is constructed with the same selection criteria for the B_{tag} candidate. It is used to calculate a set of continuum suppression variables consisting of CLEO cones [21], modified Fox-Wolfram moments [22] and thrust information. These variables are used as input for a boosted decision tree (BDT) to separate $B\overline{B}$ from continuum events. We use the BDT algorithm implemented in the `FastBDT` library [23].

To further reject backgrounds from leptons of secondary decays, misidentified hadrons or continuum events, a cut-based approach is chosen.

Secondary leptons and hadronic fakes are reduced by selecting signal lepton candidates passing $p^*_\ell > 0.8\,\mathrm{GeV}/c$. To improve the purity of the tag-side reconstruction, we require B_{tag} candidates with $\mathcal{P}_{\mathrm{FEI}} > 0.01$ and $M_{\mathrm{bc}} > 5.27\,\mathrm{GeV}/c^2$. Continuum events are rejected by cutting on the classifier output of the continuum suppression BDT $\mathcal{P}_{\mathrm{CS}}$. We select candidates with $\mathcal{P}_{\mathrm{CS}} > 0.7$. To improve the quality of the reconstructed X-system, we require the absolute value of the total charge of the reconstructed event $Q_{\mathrm{tot}} = Q_{B_{\mathrm{tag}}} + Q_\ell + Q_X$ to be less than or equal to one, explicitly allowing a charge imbalance. Further, the X-system is required to contain at least one charged particle. The missing momentum p_{miss} and missing energy E_{miss} are required to be greater than $0.5\,\mathrm{GeV}/c$ and $0.5\,\mathrm{GeV}$, respectively. The absolute value of $E_{\mathrm{miss}} - c \cdot p_{\mathrm{miss}}$ should be smaller than $0.5\,\mathrm{GeV}$. The missing four-momentum is defined as

$$p^\mu_{\mathrm{miss}} = p^\mu_{e^+e^-} - p^\mu_{B_{\mathrm{tag}}} - p^\mu_\ell - p^\mu_X. \tag{3}$$

The event selection criteria are summarized in Table II. If multiple $B_{\mathrm{tag}}\ell$ combinations are present in an event after applying all selection criteria, a best candidate selection (BCS) based on the highest p^*_ℓ is performed. In the case where the same lepton is combined with two different tag-side candidates, the B_{tag} candidate with the smallest ΔE is chosen.

Figure 1 shows the reconstructed M_X distribution for the full recorded data set with a total integrated luminosity of $34.6\,\mathrm{fb}^{-1}$. The displayed MC sample corresponds to an integrated luminosity of $100\,\mathrm{fb}^{-1}$ and has been scaled to match the luminosity of the recorded data set. The MC components are corrected for differences in PID and FEI efficiencies between data and simulation. We correct fake lepton candidates matched to a π particle on MC level. The FEI correction factors for the $B\overline{B}$ components are determined in Ref. [24], while the correction factors for the continuum component are determined in the side-band of the continuum suppression BDT.

TABLE II: Event selection criteria applied to the reconstructed $\Upsilon(4S)$ candidates.

Variable	Applied Cut Value
p^*_ℓ	$> 0.8\,\mathrm{GeV}/c$
M_{bc}	$> 5.27\,\mathrm{GeV}/c^2$
$\mathcal{P}_{\mathrm{FEI}}$	> 0.01
$\mathcal{P}_{\mathrm{CS}}$	> 0.7
$\lvert Q_{\mathrm{tot}}\rvert$	≤ 1
$N_{\mathrm{tracks,X}}$	≥ 1
E_{miss}	$> 0.5\,\mathrm{GeV}$
p_{miss}	$> 0.5\,\mathrm{GeV}/c$
$\lvert E_{\mathrm{miss}} - c \cdot p_{\mathrm{miss}}\rvert$	$< 0.5\,\mathrm{GeV}$

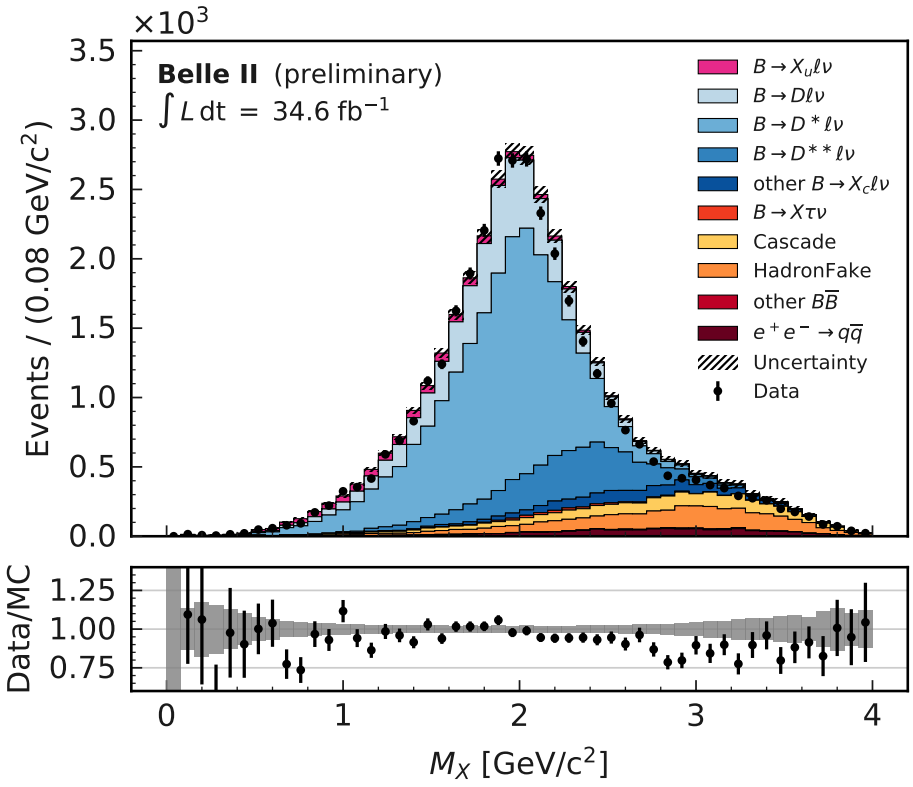

FIG. 1: Reconstructed M_X distribution with event selection criteria and BCS applied. The uncertainty band covers the MC statistics, signal lepton PID efficiency and pion fake rate correction, and the FEI efficiency correction for $B\overline{B}$ and continuum events. At the bottom the per bin ratio of data and MC is shown. The grey boxes display the ratio between the MC expectation taking into account its uncertainty and the nominal value.

4. BACKGROUND SUBTRACTION

The calculation of the hadronic mass moments of $B \to X_c \ell \nu_\ell$ decays requires the subtraction of the remaining background components from the measured events. To verify the description of the background components in MC, the background enriched reconstruction channels $B^+_{\mathrm{tag}}\ell^+$ are used. A two component template fit of the M_X distribution is used to determine the number of

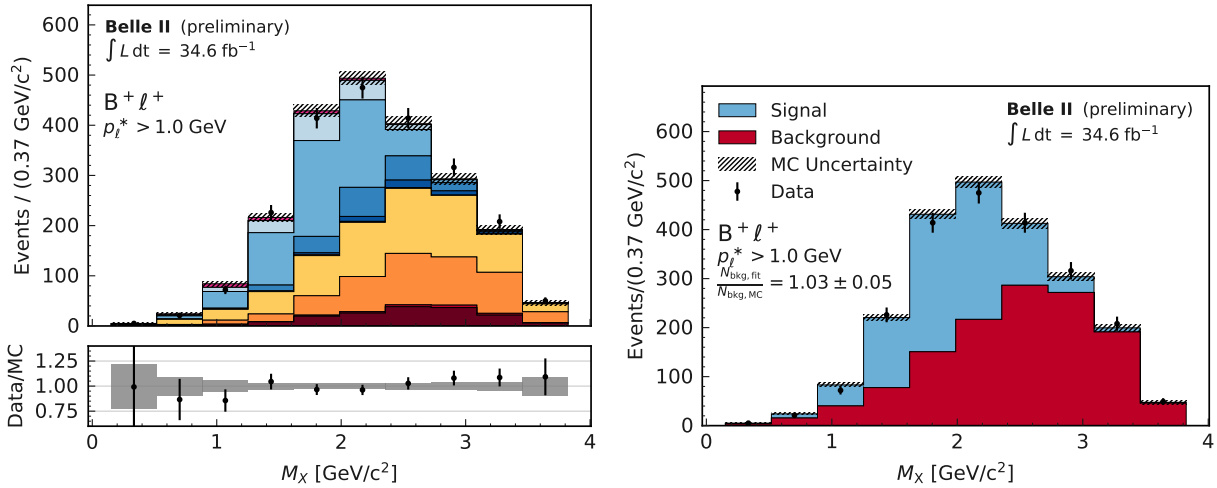

FIG. 2: M_X distribution in the $B^+\ell^+$ channels for a lower limit of $p^*_\ell > 1.0\,\mathrm{GeV}/c$. The pre-fit M_X spectrum split into sub-components and the post-fit distribution of the two component template fit are shown in the left and right plot, respectively.

background events in data. The background component yield is fitted, while the normalization of the signal template is fixed. This check is performed for different lower limits on p^*_ℓ. The ratio of the fitted number of background events to the MC expectation is compatible to unity for all lower p^*_ℓ cuts. Figure 2 shows the pre-fit M_X spectrum split into sub-components in the $B^+_{\mathrm{tag}}\ell^+$ channel for a lower limit on the lepton momentum of $p^*_\ell > 1.0\,\mathrm{GeV}/c$ as well as the post-fit distribution of the signal and background fit.

We subtract the background by assigning a signal probability to each event. The signal probability $w_i(M_X)$ is determined from a fit of the bin-wise difference between the measured M_X spectrum and the remaining background MC components normalized to the measured distribution

$$w_i(M_X) = \frac{N_i^{\mathrm{data}} - N_i^{\mathrm{bkg,MC}}}{N_i^{\mathrm{data}}}, \tag{4}$$

where the index i denotes the corresponding M_X bin. To get a continuous description of the signal probability, we fit a series of Legendre polynomials to the bin-wise probabilities. Prior to fitting, the fit-range is transformed to the interval $[-1, 1]$ to exploit the orthogonal nature of the polynomials. The order of the Legendre polynomial is determined by cutting off the series when the next higher order fitted coefficient is compatible with zero. If the fit reaches a minimum in the background dominated low or high hadronic mass values, the polynomial is replaced by a constant value equal to the found minimum. The procedure is performed for different lower limits on the lepton momentum p^*_ℓ. Figure 3 shows the fitted signal probability as a function of the reconstructed M_X with $p^*_\ell > 0.8\,\mathrm{GeV}/c$ and the measured M_X spectrum compared to the background MC components.

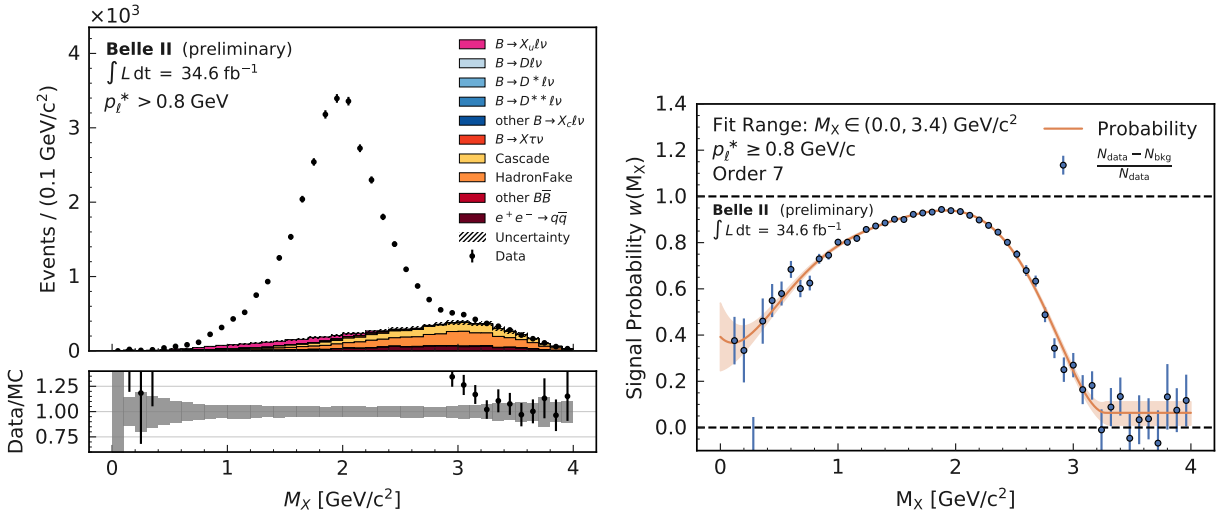

FIG. 3: The left column shows the M_X distribution in data and background MC (normalized to the events in data) for $p_\ell^* > 0.8\,\mathrm{GeV}/c$. The corresponding background subtraction factors w_i are shown in the right column together with a fitted Legendre polynomial of degree 7. If the fit has a minimum at the left or right tail, the polynomial is replaced with a constant value. The uncertainties are from statistical uncertainties only.

5. MEASUREMENT OF HADRONIC MASS MOMENTS

5.1. Extraction of Moments

To extract unbiased moments, the measured M_X^n spectrum has to be corrected for effects that distort the measured distribution. We derive calibration functions based on MC simulation to describe the relationship between the reconstructed moments $\langle M_{X,\mathrm{reco}}^n \rangle$ and the moments calculated at the generator level $\langle M_{X,\mathrm{true}}^n \rangle$. Both moments are calculated in bins of the generator level M_X^n distribution. We find a linear relationship between $\langle M_{X,\mathrm{reco}}^n \rangle$ and $\langle M_{X,\mathrm{true}}^n \rangle$, which allows us to calculate a calibrated M_X value

$$M_{X,\mathrm{calib}}^n = \frac{M_X^n - c(E_{\mathrm{miss}} - p_{\mathrm{miss}}, \mathrm{X_{mult}}, p_\ell^*)}{m(E_{\mathrm{miss}} - p_{\mathrm{miss}}, \mathrm{X_{mult}}, p_\ell^*)} \,. \tag{5}$$

Here c and m denote the fitted intercept and slope of the linear calibration functions, respectively. Since the bias of the measured M_X spectrum is not constant over the available phase-space, the calibration is performed in bins of p_ℓ^*, $E_{\mathrm{miss}} - p_{\mathrm{miss}}$, and the particle multiplicity of the X-system denoted as $\mathrm{X_{mult}}$. We use bins in p_ℓ^* with a width of $0.1\,\mathrm{GeV}/c$ between 0.8 and $1.9\,\mathrm{GeV}/c$ and one bin for $p_\ell^* \geq 1.9\,\mathrm{GeV}/c$. A binning of $[-0.5, 0.05, 0.2, 0.5]$ GeV and $[1, 8, 30]$ is used for $E_{\mathrm{miss}} - c \cdot p_{\mathrm{miss}}$ and $\mathrm{X_{mult}}$, respectively. Due to limited statistics in the phase space above $p_\ell^* \geq 1.7\,\mathrm{GeV}/c$, the additional binning in $E_{\mathrm{miss}} - c \cdot p_{\mathrm{miss}}$ and $\mathrm{X_{mult}}$ is not used in this region. Figure 4 shows an example of three calibration curves for $\langle M_X \rangle$ in three bins of p_ℓ^* and one bin in $E_{\mathrm{miss}} - c \cdot p_{\mathrm{miss}}$ and $\mathrm{X_{mult}}$. Figure 5 shows the second hadronic mass moment $\langle M_X^2 \rangle$ from signal MC before and after the application of the calibration procedure. The second moments of the $B \to X_c \ell \nu_\ell$ MC at generator level with and without the application of event selection criteria are also shown.

Together with the signal probability w_i and the calibrated $M_{X,\mathrm{calib}}$ distribution, the $\langle M_X^n \rangle$ can be calculated without unfolding the measured M_X spectrum. The hadronic mass moments are

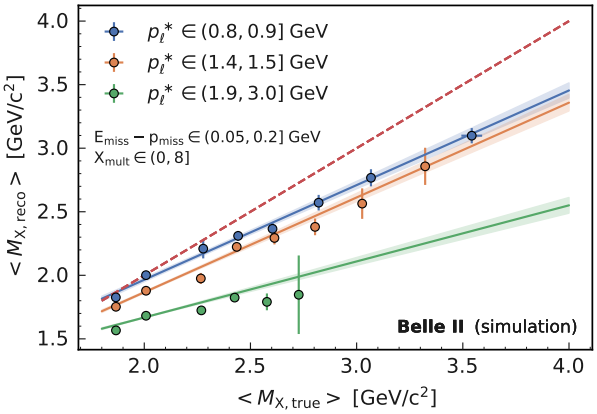

FIG. 4: Example of the calibration curves for the first moment $\langle M_X \rangle$ in bins of $E_{\text{miss}} - p_{\text{miss}}$, X_{mult} and p_ℓ^*. The moments $\langle M_{X,\text{reco}} \rangle$ versus $\langle M_{X,\text{true}} \rangle$ calculated in bins of $M_{X,\text{true}}$ are shown. The uncertainty of the calibration curves takes into account the statistical uncertainty on the fitted slope and intercept. The red dashed reference line shows $\langle M_{X,\text{true}} \rangle = \langle M_{X,\text{reco}} \rangle$

calculated as a weighted average using

$$\langle M_X^n \rangle = \frac{\sum_i w_i(M_X) M_{X,\text{calib}i}^{\ n}}{\sum_i w_i(M_X)} \times \mathcal{C}_{\text{calib}} \times \mathcal{C}_{\text{true}}. \tag{6}$$

The two additional factors $\mathcal{C}_{\text{calib}}$ and $\mathcal{C}_{\text{true}}$ correct a remaining bias due to the calibration and selection efficiencies for different $B \to X_c \ell \nu_\ell$ components. The factor $\mathcal{C}_{\text{calib}} = \langle M_{X,\text{true}}^n \rangle / \langle M_{X,\text{calib}}^n \rangle$ corrects the remaining bias of the calibrated moments and the true moments for each lower limit on p_ℓ^*. We observe remaining bias corrections ranging between 1.001 for the first moment up to 0.988 for the fourth moment. To correct a possible bias due to the event selection criteria applied, we apply a second correction factor $\mathcal{C}_{\text{true}} = \langle M_{X,\text{true,signal}}^n \rangle / \langle M_{X,\text{true}}^n \rangle$. Here, $\langle M_{X,\text{true,signal}}^n \rangle$ are the moments of the generator M_X spectrum of our simulated $B \to X_c \ell \nu_\ell$ decays without the application of the aforementioned event selection criteria. Only a cut on the generator level lepton momentum in the signal B meson rest frame is applied. To be able to correct for the effect of final state radiation on the lepton momentum, the MC sample used to calculate $\langle M_{X,\text{true,signal}}^n \rangle$ does not include the simulation of radiative photons with `PHOTOS`. We obtain values for $\mathcal{C}_{\text{true}}$ ranging from 1.02 to 1.27 for the lowest p_ℓ^* cut. For higher p_ℓ^* cuts the $\mathcal{C}_{\text{true}}$ ranges from 1.00 to 1.01 for the highest cut value.

5.2. Uncertainties

We identify several sources of statistical and systematic uncertainties. The total uncertainty is calculated by adding statistical and systematic uncertainties in quadrature.

For the statistical uncertainty, we consider two different components. The $\langle M_X^n \rangle$ are calculated as a weighted mean over all events. We calculated the variance of the weighted mean as [25]

$$V(\langle M_X^n \rangle) = \frac{n}{(n-1)\sum_i^n w_i} \sum_i^n w_i^2 (M_{X,\text{calib},i}^n - \langle M_X^n \rangle)^2. \tag{7}$$

We verified the validity of this formula applying a bootstrapping approach. The second part of the statistical uncertainty is given by the statistical uncertainty of the polynomial coefficients of the signal probability function. The uncertainty is propagated by using error propagation to calculate

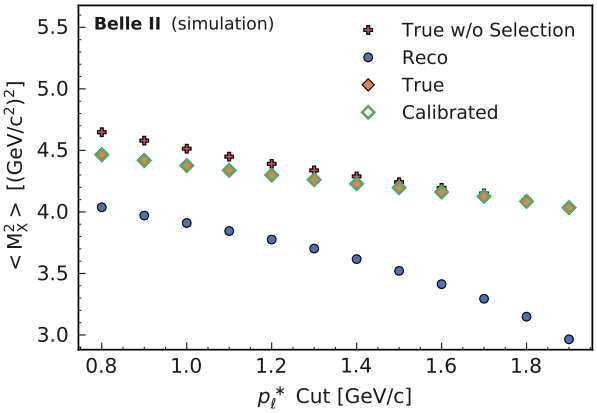

FIG. 5: Second hadronic mass moment $\langle M_X^2 \rangle$ calculated on signal MC for different lower limits on p_ℓ^*. The plotted moments are the measured uncalibrated, calibrated and true moments after the application of all analysis selection criteria. In addition, the true $\langle M_X^2 \rangle$ calculated from the MC sample without any selection criteria applied are shown as red crosses.

the uncertainty on the signal probability. To estimate the impact of the propagated uncertainty on the measured $\langle M_X^n \rangle$, the calculation of the moments is repeated with varied signal probability values. The total statistical uncertainty is calculated by summing both uncertainties in quadrature.

To estimate the impact of systematic uncertainties, the following effects are taken into account:

1. Statistical uncertainty on the linear calibration functions:
   The used linear calibration functions are determined using a dedicated MC sample of $B \to X_c \ell \nu_\ell$ decays. Both the slope and the intercept have statistical uncertainties and are correlated. To propagate the uncertainties correctly with their correlations, the eigenvalues and eigenvectors of the covariance matrix are used to calculate two orthogonal variations of both parameters via

$$c_i^{\pm} = c_i^{nom} \pm \sqrt{\lambda_i} \hat{e}_i, \tag{8}$$

   where c_i^{nom} and $c_i^{\pm}$ denote the nominal and varied parameters, respectively, of the linear calibration function. λ_i and $\hat{e}_i$ are the i-th eigenvalue and eigenvector of the parameter covariance matrix. In total, we get two ($i = 1, 2$) independent variations of the determined parameters.

   The impact of these uncertainties is estimated by repeating the calculation of the M_X moments and taking the total value of the difference of each variation divided by two as a source of uncertainty. A larger set of MC events would reduce this systematic.

2. FEI and PID efficiency correction uncertainty:
   The FEI efficiency correction uncertainty is propagated by varying the efficiency correction by its uncertainty and repeating the determination of the background subtraction weights. Again, the uncertainty is taken as half of the total value of the resulting difference of $\langle M_X^n \rangle$ calculated with varied probabilities.

   The PID uncertainty is estimated using the set of varied nominal weights in bins of M_X. The PID correction for each event is varied by the estimated bin-wise uncertainty. To gauge the impact of this source of uncertainty, the same method as for the FEI efficiency uncertainty determination is used.

3. $B \to X_u \ell \nu_\ell$ branching fraction uncertainty:
The $B \to X_u \ell \nu_\ell$ branching fraction uncertainty is estimated to be 14% using the latest experimental average of $(2.13 \pm 0.30)\,\%$ [26]. The corresponding MC component is varied accordingly and the signal probability function is redetermined using the varied MC sample.

4. Statistical uncertainty on the bias correction factor $\mathcal{C}_{\text{calib}} \times \mathcal{C}_{\text{true}}$:
The remaining bias correction also contains a statistical uncertainty due to the limited number of MC events used to determine it. The M_X moments are calculated by varying the bias correction factor according to this statistical uncertainty.

5. Composition of higher mass X_c states:
The bias correction factor $\mathcal{C}_{\text{true}}$ yields a significant correction to the final result. The origin of this correction is the underlying modeling of the higher mass states of the $B \to X_c \ell \nu_\ell$ spectrum, which has changed in comparison to previous analyses. The uncertainty of this correction factor is determined by assigning a 100% uncertainty to the branching fraction of the non-resonant part of the X_c spectrum and repeating the calculation for $\mathcal{C}_{\text{true}}$. The 100% uncertainty on the non-resonant $B \to X_c \ell \nu_\ell$ branching fractions is a conservative choice, since the decays contributing to this region of the spectrum are not determined experimentally. The resulting uncertainty is propagated to the $\langle M_X^n \rangle$ values by repeating the calculation with the varied $\mathcal{C}_{\text{true}}$ and taking the absolute value of the difference to the nominal moments as the systematic uncertainty.

To estimate the total systematic uncertainty, all considered sources of systematics are added in quadrature.

5.3. Results

The measured hadronic mass moments are shown in Figure 6 as a function of a lower limit on the lepton momentum in the signal B rest frame. The results of previous analyses performed by BaBar [27] and Belle [28] are shown for comparison. The results agree within the uncertainties, but the current precision is not yet competitive. The numerical values, together with the itemization of the full statistical and systematic uncertainties, are given in Appendix A. The measured moments show a clear dependence on the p_ℓ^* cut, resulting in smaller $\langle M_X^n \rangle$ values for higher p_ℓ^* cuts. The uncertainties of the moments for lower p_ℓ^* cuts are dominated by the systematic components, while those for higher p_ℓ^* cuts have a higher statistical uncertainty.

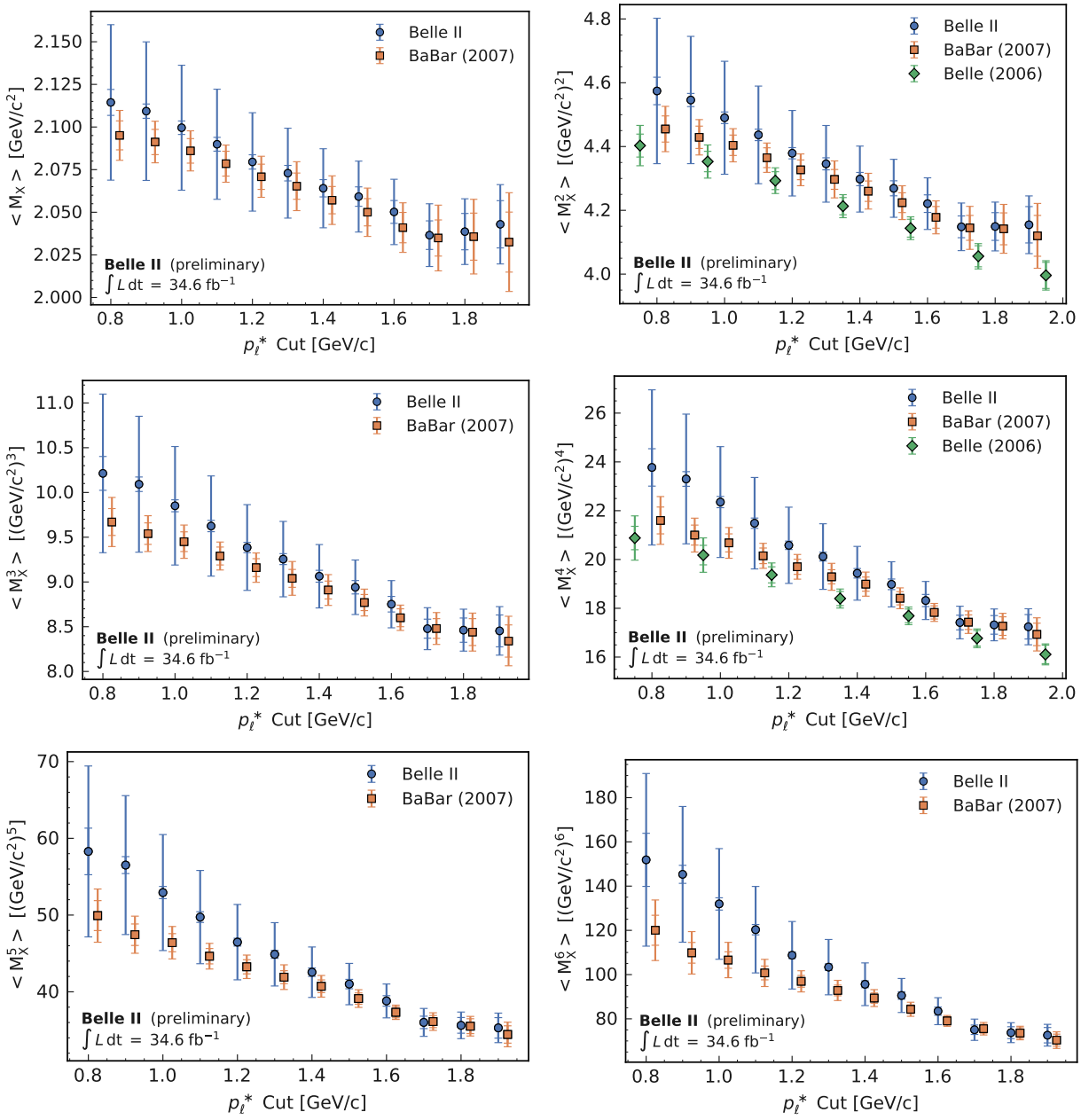

FIG. 6: Measured $\langle M_X^n \rangle$ moments as a function of different p_ℓ^* cuts. The error-bars correspond to the statistical (inner) and total (outer) uncertainty calculated by adding the statistical and systematic error in quadrature. A comparison to previous $\langle M_X^n \rangle$ measurements from BaBar (2007) and Belle (2006) is shown as reference points. The current precision is not yet competitive with the previous results.

6. SUMMARY

We have presented a preliminary measurement the first six moments of the hadronic mass spectrum in $B \to X_c \ell \nu_\ell$ decays. The $\langle M_X^n \rangle$ are measured as a function of a lower cut on the lepton momentum in the signal B rest frame p_ℓ^*. The results agree with previous measurements within their uncertainties, but tend to higher nominal values for lower cuts on p_ℓ^*. The moments are calculated as a weighted mean using signal probabilities as event-wise weights. The achieved precision is not

yet competitive with previous analyses. The systematic uncertainties, in particular, can decrease in futures measurements by reducing the bias in the reconstructed M_X distribution as well as more extensive studies on the composition of unmeasured parts of the $B \to X_c \ell \nu_\ell$ spectrum.

Acknowledgements

We thank the SuperKEKB group for the excellent operation of the accelerator; the KEK cryogenics group for the efficient operation of the solenoid; and the KEK computer group for on-site computing support. This work was supported by the following funding sources: Science Committee of the Republic of Armenia Grant No. 18T-1C180; Australian Research Council and research grant Nos. DP180102629, DP170102389, DP170102204, DP150103061, FT130100303, and FT130100018; Austrian Federal Ministry of Education, Science and Research, and Austrian Science Fund No. P 31361-N36; Natural Sciences and Engineering Research Council of Canada, Compute Canada and CANARIE; Chinese Academy of Sciences and research grant No. QYZDJ-SSW-SLH011, National Natural Science Foundation of China and research grant Nos. 11521505, 11575017, 11675166, 11761141009, 11705209, and 11975076, LiaoNing Revitalization Talents Program under contract No. XLYC1807135, Shanghai Municipal Science and Technology Committee under contract No. 19ZR1403000, Shanghai Pujiang Program under Grant No. 18PJ1401000, and the CAS Center for Excellence in Particle Physics (CCEPP); the Ministry of Education, Youth and Sports of the Czech Republic under Contract No. LTT17020 and Charles University grants SVV 260448 and GAUK 404316; European Research Council, 7th Framework PIEF-GA-2013-622527, Horizon 2020 Marie Sklodowska-Curie grant agreement No. 700525 'NIOBE,' and Horizon 2020 Marie Sklodowska-Curie RISE project JENNIFER2 grant agreement No. 822070 (European grants); L'Institut National de Physique Nucléaire et de Physique des Particules (IN2P3) du CNRS (France); BMBF, DFG, HGF, MPG, AvH Foundation, and Deutsche Forschungsgemeinschaft (DFG) under Germany's Excellence Strategy – EXC2121 "Quantum Universe"' – 390833306 (Germany); Department of Atomic Energy and Department of Science and Technology (India); Israel Science Foundation grant No. 2476/17 and United States-Israel Binational Science Foundation grant No. 2016113; Istituto Nazionale di Fisica Nucleare and the research grants BELLE2; Japan Society for the Promotion of Science, Grant-in-Aid for Scientific Research grant Nos. 16H03968, 16H03993, 16H06492, 16K05323, 17H01133, 17H05405, 18K03621, 18H03710, 18H05226, 19H00682, 26220706, and 26400255, the National Institute of Informatics, and Science Information NETwork 5 (SINET5), and the Ministry of Education, Culture, Sports, Science, and Technology (MEXT) of Japan; National Research Foundation (NRF) of Korea Grant Nos. 2016R1D1A1B01010135, 2016R1D1A1B02012900, 2018R1A2B3003643, 2018R1A6A1A06024970, 2018R1D1A1B07047294, 2019K1A3A7A09033840, and 2019R1I1A3A01058933, Radiation Science Research Institute, Foreign Large-size Research Facility Application Supporting project, the Global Science Experimental Data Hub Center of the Korea Institute of Science and Technology Information and KREONET/GLORIAD; Universiti Malaya RU grant, Akademi Sains Malaysia and Ministry of Education Malaysia; Frontiers of Science Program contracts FOINS-296, CB-221329, CB-236394, CB-254409, and CB-180023, and SEP-CINVESTAV research grant 237 (Mexico); the Polish Ministry of Science and Higher Education and the National Science Center; the Ministry of Science and Higher Education of the Russian Federation, Agreement 14.W03.31.0026; University of Tabuk research grants S-1440-0321, S-0256-1438, and S-0280-1439 (Saudi Arabia); Slovenian Research Agency and research grant Nos. J1-9124 and P1-0135; Agencia Estatal de Investigacion, Spain grant Nos. FPA2014-55613-P and FPA2017-84445-P, and CIDEGENT/2018/020 of Generalitat Valenciana; Ministry of Science and Technology and research grant Nos. MOST106-2112-M-002-005-MY3 and MOST107-2119-M-002-035-MY3, and the Ministry of Education (Taiwan); Thailand Center of Excellence in Physics; TUBITAK ULAKBIM

(Turkey); Ministry of Education and Science of Ukraine; the US National Science Foundation and research grant Nos. PHY-1807007 and PHY-1913789, and the US Department of Energy and research grant Nos. DE-AC06-76RLO1830, DE-SC0007983, DE-SC0009824, DE-SC0009973, DE-SC0010073, DE-SC0010118, DE-SC0010504, DE-SC0011784, DE-SC0012704; and the National Foundation for Science and Technology Development (NAFOSTED) of Vietnam under contract No 103.99-2018.45.

---

[1] P. Gambino et al., *Challenges in Semileptonic B Decays*, arXiv:2006.07287.

[2] T. Keck et al., *The Full Event Interpretation*, Computing and Software for Big Science **3** (Feb, 2019) . http://dx.doi.org/10.1007/s41781-019-0021-8.

[3] T. Abe, Belle II Collaboration, *Belle II Technical Design Report*, arXiv:1011.0352.

[4] K. Akai et al., SuperKEKB, *SuperKEKB Collider*, Nucl. Instrum. Meth. A **907** (2018) 188–199, arXiv:1809.01958.

[5] W. Altmannshofer et al., Belle-II, *The Belle II Physics Book*, PTEP **2019** (2019) no. 12, 123C01, arXiv:1808.10567. [Erratum: PTEP 2020, 029201 (2020)].

[6] D. Lange, *The EvtGen particle decay simulation package*, Nuclear Instruments and Methods in Physics Research Section A: Accelerators, Spectrometers, Detectors and Associated Equipment **462** (2001) no. 1, 152 – 155. http://www.sciencedirect.com/science/article/pii/S0168900201000894. BEAUTY2000, Proceedings of the 7th Int. Conf. on B-Physics at Hadron Machines.

[7] S. Agostinelli et al., GEANT4, *GEANT4: A Simulation toolkit*, Nucl.Instrum.Meth. **A506** (2003) 250–303.

[8] E. Barberio et al., *Photos — a universal Monte Carlo for QED radiative corrections in decays*, Computer Physics Communications **66** (1991) no. 1, 115 – 128. http://www.sciencedirect.com/science/article/pii/001046559190012A.

[9] B. Ward, S. Jadach, and Z. Was, *Precision calculation for e+ e- —¿ 2f: The KK MC project*, Nucl. Phys. B Proc. Suppl. **116** (2003) 73–77, arXiv:hep-ph/0211132.

[10] T. Sjöstrand et al., *A brief introduction to PYTHIA 8.1*, Computer Physics Communications **178** (Jun, 2008) 852–867. http://dx.doi.org/10.1016/j.cpc.2008.01.036.

[11] T. Kuhr, C. Pulvermacher, M. Ritter, T. Hauth, and N. Braun, Belle-II Framework Software Group, *The Belle II Core Software*, Comput. Softw. Big Sci. **3** (2019) no. 1, 1, arXiv:1809.04299.

[12] V. Bertacchi et al., Belle II Tracking, *Track Finding at Belle II*, arXiv:2003.12466.

[13] C. Boyd et al., *Precision corrections to dispersive bounds on form factors*, Physical Review D **56** (Dec, 1997) 6895–6911. http://dx.doi.org/10.1103/PhysRevD.56.6895.

[14] R. Glattauer et al., Belle, *Measurement of the decay $B \to D\ell\nu_\ell$ in fully reconstructed events and determination of the Cabibbo-Kobayashi-Maskawa matrix element $|V_{cb}|$*, Physical Review D **93** (Feb, 2016) . http://dx.doi.org/10.1103/PhysRevD.93.032006.

[15] I. Caprini et al., *Dispersive bounds on the shape of $B \to D^* \ell \bar{\nu}_\ell$ form factors*, Nuclear Physics B **530** (1998) no. 1, 153 – 181.

[16] Y. Amhis et al., *Averages of b-hadron, c-hadron, and τ-lepton properties as of summer 2016*, The European Physical Journal C **77** (Dec, 2017) .

[17] A. Leibovich et al., *Semileptonic B decays to excited charmed mesons*, Physical Review D **57** (Jan, 1998) 308–330. http://dx.doi.org/10.1103/PhysRevD.57.308.

[18] F. Bernlochner and Z. Ligeti, *Semileptonic B(s) decays to excited charmed mesons with e, μ, τ and searching for new physics with $R(D^{**})$*, Physical Review D **95** (Jan, 2017) . http://dx.doi.org/10.1103/PhysRevD.95.014022.

[19] J. Goity and W. Roberts, *Soft pion emission in semileptonic B-meson decays*, Physical Review D **51** (Apr, 1995) 3459–3477. http://dx.doi.org/10.1103/PhysRevD.51.3459.

[20] G. C. Fox and S. Wolfram, *Observables for the Analysis of Event Shapes in e+ e- Annihilation and Other Processes*, Phys. Rev. Lett. **41** (1978) 1581.

[21] D. Asner et al., *Search for exclusive charmless hadronic B decays*, Phys. Rev. D **53** (Feb, 1996) 1039–1050.

[22] A. J. Bevan et al., *The Physics of the B Factories*, The European Physical Journal C **74** (Nov, 2014) .

http://dx.doi.org/10.1140/epjc/s10052-014-3026-9.
[23] T. Keck, *FastBDT: A Speed-Optimized Multivariate Classification Algorithm for the Belle II Experiment*, Comput. Softw. Big Sci. **1** (2017) no. 1, 2. https://doi.org/10.1007/s41781-017-0002-8.
[24] W. Sutcliffe, *Performance of Full Event Interpretation and a calibration with $B \to X\ell\nu$ decays in early phase III data*, Internal Note (Jul, 2019) .
[25] D. Gatz and L. Smith, *The standard error of a weighted mean concentration—I. Bootstrapping vs other methods*, Atmospheric Environment **29** (1995) no. 11, 1185 – 1193. http://www.sciencedirect.com/science/article/pii/135223109400210C.
[26] M. Tanabashi et al., Particle Data Group, *Review of Particle Physics*, Phys. Rev. D **98** (Aug, 2018) 030001.
[27] BaBar, B. Aubert et al., *Measurement of moments of the hadronic-mass and energy spectrum in inclusive semileptonic $B \to X_c\ell\nu_\ell$*, in *2007 Europhysics Conference on High Energy Physics*. 7, 2007. arXiv:0707.2670.
[28] C. Schwanda et al., Belle, *Moments of the hadronic invariant mass spectrum in $B \to X_c\ell\nu_\ell$ decays at Belle*, Physical Review D **75** (Feb, 2007) . http://dx.doi.org/10.1103/PhysRevD.75.032005.

APPENDIX A: NUMERICAL RESULTS AND BREAKDOWN OF STATISTICAL AND SYSTEMATIC UNCERTAINTIES

TABLE III: Summary of statistical and systematic uncertainties for the measurement of $\langle M_X \rangle$. All values are given in GeV/c1 if not stated otherwise. The calculation of the uncertainties is described in Section 5 5.2.

p_ℓ^* Cut in GeV/c	0.8	0.9	1.0	1.1	1.2	1.3
$\langle M_X \rangle$ in GeV/c1	2.1144	2.1093	2.0996	2.0899	2.0795	2.0729
Stat. error (data)	0.0035	0.0036	0.0038	0.0039	0.0042	0.0045
Stat. error (signal prob.)	0.0068	0.0021	0.0013	0.0009	0.0000	0.0003
Stat. error (total)	0.0076	0.0042	0.0040	0.0040	0.0042	0.0045
Calib. function error	0.0107	0.0102	0.0099	0.0096	0.0093	0.0090
Fei eff.	0.0059	0.0035	0.0020	0.0009	0.0000	0.0004
PID eff.	0.0086	0.0042	0.0032	0.0022	0.0013	0.0011
$B \to X_u \ell \nu_\ell$ BF	0.0042	0.0041	0.0040	0.0041	0.0042	0.0044
Bias corr. (stat)	0.0025	0.0025	0.0025	0.0025	0.0026	0.0027
Bias corr. (model)	0.0421	0.0384	0.0345	0.0301	0.0265	0.0237
Sys. error (total)	0.0449	0.0404	0.0364	0.0320	0.0285	0.0260
Total error	0.0456	0.0406	0.0366	0.0323	0.0289	0.0264
p_ℓ^* Cut in GeV/c	1.4	1.5	1.6	1.7	1.8	1.9
$\langle M_X \rangle$ in GeV/c1	2.0641	2.0592	2.0502	2.0366	2.0386	2.0429
Stat. error (data)	0.0050	0.0057	0.0066	0.0082	0.0103	0.0132
Stat. error (signal prob.)	0.0008	0.0007	0.0009	0.0018	0.0028	0.0042
Stat. error (total)	0.0051	0.0057	0.0067	0.0084	0.0107	0.0139
Calib. function error	0.0088	0.0086	0.0083	0.0074	0.0077	0.0076
Fei eff.	0.0008	0.0012	0.0015	0.0019	0.0026	0.0037
PID eff.	0.0009	0.0008	0.0009	0.0011	0.0014	0.0019
$B \to X_u \ell \nu_\ell$ BF	0.0048	0.0054	0.0067	0.0083	0.0101	0.0142
Bias corr. (stat)	0.0029	0.0033	0.0037	0.0045	0.0057	0.0075
Bias corr. (model)	0.0200	0.0168	0.0139	0.0109	0.0074	0.0042
Sys. error (total)	0.0226	0.0200	0.0180	0.0164	0.0161	0.0187
Total error	0.0232	0.0208	0.0192	0.0184	0.0193	0.0233

TABLE IV: Summary of statistical and systematic uncertainties for the measurement of $\langle M_X^2 \rangle$. All values are given in $(\mathrm{GeV}/c1)^2$ if not stated otherwise. The calculation of the uncertainties is described in Section 5 5.2.

p_ℓ^* Cut in GeV/c	0.8	0.9	1.0	1.1	1.2	1.3
$\langle M_X^2 \rangle$ in $(\mathrm{GeV}/c1)^2$	4.5743	4.5459	4.4902	4.4365	4.3790	4.3458
Stat. error (data)	0.0146	0.0151	0.0157	0.0165	0.0175	0.0189
Stat. error (signal prob.)	0.0405	0.0140	0.0092	0.0071	0.0017	0.0003
Stat. error (total)	0.0431	0.0206	0.0182	0.0180	0.0176	0.0189
Calib. function error	0.0473	0.0447	0.0427	0.0410	0.0393	0.0380
Fei eff.	0.0340	0.0201	0.0118	0.0060	0.0014	0.0005
PID eff.	0.0476	0.0210	0.0164	0.0109	0.0060	0.0046
$B \to X_u \ell \nu_\ell$ BF	0.0168	0.0157	0.0151	0.0150	0.0153	0.0160
Bias corr. (stat)	0.0115	0.0112	0.0110	0.0110	0.0112	0.0116
Bias corr. (model)	0.2099	0.1902	0.1687	0.1446	0.1254	0.1106
Sys. error (total)	0.2239	0.1985	0.1762	0.1519	0.1329	0.1187
Total error	0.2280	0.1996	0.1771	0.1530	0.1340	0.1202
p_ℓ^* Cut in GeV/c	1.4	1.5	1.6	1.7	1.8	1.9
$\langle M_X^2 \rangle$ in $(\mathrm{GeV}/c1)^2$	4.2980	4.2691	4.2209	4.1483	4.1493	4.1547
Stat. error (data)	0.0208	0.0235	0.0274	0.0337	0.0426	0.0553
Stat. error (signal prob.)	0.0011	0.0017	0.0026	0.0054	0.0088	0.0137
Stat. error (total)	0.0208	0.0236	0.0275	0.0341	0.0435	0.0570
Calib. function error	0.0366	0.0355	0.0339	0.0296	0.0310	0.0303
Fei eff.	0.0020	0.0038	0.0050	0.0065	0.0092	0.0134
PID eff.	0.0037	0.0032	0.0035	0.0041	0.0051	0.0070
$B \to X_u \ell \nu_\ell$ BF	0.0171	0.0200	0.0228	0.0283	0.0358	0.0503
Bias corr. (stat)	0.0123	0.0135	0.0154	0.0184	0.0230	0.0303
Bias corr. (model)	0.0920	0.0764	0.0621	0.0483	0.0328	0.0185
Sys. error (total)	0.1013	0.0878	0.0761	0.0664	0.0629	0.0703
Total error	0.1034	0.0909	0.0810	0.0746	0.0765	0.0905

TABLE V: Summary of statistical and systematic uncertainties for the measurement of $\langle M_X^3 \rangle$. All values are given in $(\mathrm{GeV}/c1)^3$ if not stated otherwise. The calculation of the uncertainties is described in Section 5 5.2.

p_ℓ^* Cut in GeV/c	0.8	0.9	1.0	1.1	1.2	1.3
$\langle M_X^3 \rangle$ in $(\mathrm{GeV}/c1)^3$	10.2132	10.0919	9.8513	9.6251	9.3849	9.2553
Stat. error (data)	0.0475	0.0492	0.0509	0.0534	0.0564	0.0608
Stat. error (signal prob.)	0.1830	0.0645	0.0431	0.0344	0.0108	0.0054
Stat. error (total)	0.1891	0.0811	0.0667	0.0635	0.0574	0.0610
Calib. function error	0.1668	0.1556	0.1463	0.1383	0.1302	0.1250
Fei eff.	0.1493	0.0875	0.0517	0.0273	0.0088	0.0019
PID eff.	0.2065	0.0788	0.0660	0.0422	0.0210	0.0153
$B \to X_u \ell \nu_\ell$ BF	0.0535	0.0485	0.0448	0.0435	0.0435	0.0452
Bias corr. (stat)	0.0429	0.0407	0.0391	0.0382	0.0377	0.0384
Bias corr. (model)	0.8077	0.7266	0.6339	0.5331	0.4533	0.3929
Sys. error (total)	0.8659	0.7550	0.6586	0.5560	0.4756	0.4168
Total error	0.8863	0.7594	0.6620	0.5596	0.4791	0.4213
p_ℓ^* Cut in GeV/c	1.4	1.5	1.6	1.7	1.8	1.9
$\langle M_X^3 \rangle$ in $(\mathrm{GeV}/c1)^3$	9.0639	8.9409	8.7514	8.4779	8.4616	8.4534
Stat. error (data)	0.0664	0.0749	0.0867	0.1056	0.1339	0.1746
Stat. error (signal prob.)	0.0016	0.0030	0.0055	0.0116	0.0210	0.0347
Stat. error (total)	0.0664	0.0750	0.0869	0.1063	0.1355	0.1780
Calib. function error	0.1186	0.1140	0.1073	0.0919	0.0961	0.0932
Fei eff.	0.0036	0.0093	0.0131	0.0175	0.0250	0.0367
PID eff.	0.0118	0.0093	0.0102	0.0118	0.0143	0.0195
$B \to X_u \ell \nu_\ell$ BF	0.0476	0.0565	0.0617	0.0761	0.0978	0.1373
Bias corr. (stat)	0.0399	0.0434	0.0487	0.0572	0.0716	0.0940
Bias corr. (model)	0.3208	0.2624	0.2100	0.1604	0.1084	0.0607
Sys. error (total)	0.3478	0.2951	0.2492	0.2090	0.1910	0.2044
Total error	0.3541	0.3045	0.2639	0.2345	0.2342	0.2711

TABLE VI: Summary of statistical and systematic uncertainties for the measurement of $\langle M_X^4 \rangle$. All values are given in $(\mathrm{GeV}/c1)^4$ if not stated otherwise. The calculation of the uncertainties is described in Section 5 5.2.

p_ℓ^* Cut in GeV/c	0.8	0.9	1.0	1.1	1.2	1.3
$\langle M_X^4 \rangle$ in $(\mathrm{GeV}/c1)^4$	23.7733	23.2997	22.3539	21.4874	20.5818	20.1196
Stat. error (data)	0.1420	0.1471	0.1516	0.1584	0.1662	0.1788
Stat. error (signal prob.)	0.7534	0.2620	0.1742	0.1397	0.0472	0.0276
Stat. error (total)	0.7667	0.3005	0.2309	0.2113	0.1728	0.1809
Calib. function error	0.5569	0.5112	0.4709	0.4359	0.4010	0.3808
Fei eff.	0.5999	0.3444	0.2012	0.1073	0.0386	0.0150
PID eff.	0.8303	0.2671	0.2454	0.1511	0.0684	0.0474
$B \to X_u \ell \nu_\ell$ BF	0.1629	0.1425	0.1257	0.1182	0.1146	0.1178
Bias corr. (stat)	0.1524	0.1406	0.1308	0.1238	0.1183	0.1178
Bias corr. (model)	2.8491	2.5472	2.1796	1.7933	1.4891	1.2646
Sys. error (total)	3.0865	2.6419	2.2597	1.8626	1.5529	1.3321
Total error	3.1803	2.6590	2.2714	1.8746	1.5624	1.3444
p_ℓ^* Cut in GeV/c	1.4	1.5	1.6	1.7	1.8	1.9
$\langle M_X^4 \rangle$ in $(\mathrm{GeV}/c1)^4$	19.4346	18.9820	18.3187	17.4161	17.3199	17.2427
Stat. error (data)	0.1935	0.2177	0.2487	0.2993	0.3791	0.4942
Stat. error (signal prob.)	0.0178	0.0026	0.0093	0.0209	0.0449	0.0801
Stat. error (total)	0.1943	0.2177	0.2488	0.3000	0.3817	0.5006
Calib. function error	0.3546	0.3360	0.3110	0.2587	0.2695	0.2597
Fei eff.	0.0032	0.0205	0.0309	0.0423	0.0619	0.0915
PID eff.	0.0343	0.0248	0.0268	0.0306	0.0367	0.0492
$B \to X_u \ell \nu_\ell$ BF	0.1218	0.1459	0.1538	0.1884	0.2431	0.3400
Bias corr. (stat)	0.1195	0.1277	0.1407	0.1615	0.2013	0.2633
Bias corr. (model)	1.0099	0.8108	0.6371	0.4755	0.3194	0.1774
Sys. error (total)	1.0844	0.8994	0.7401	0.5978	0.5286	0.5428
Total error	1.1016	0.9254	0.7808	0.6689	0.6520	0.7384

TABLE VII: Summary of statistical and systematic uncertainties for the measurement of $\langle M_X^5 \rangle$. All values are given in $(\mathrm{GeV}/c1)^5$ if not stated otherwise. The calculation of the uncertainties is described in Section 5 5.2.

p_ℓ^* Cut in GeV/c	0.8	0.9	1.0	1.1	1.2	1.3
$\langle M_X^5 \rangle$ in $(\mathrm{GeV}/c1)^5$	58.2926	56.5135	52.9344	49.7378	46.4718	44.8842
Stat. error (data)	0.4142	0.4295	0.4394	0.4566	0.4749	0.5093
Stat. error (signal prob.)	3.0074	1.0155	0.6627	0.5267	0.1790	0.1105
Stat. error (total)	3.0357	1.1026	0.7951	0.6971	0.5075	0.5211
Calib. function error	1.8603	1.6787	1.5072	1.3584	1.2127	1.1360
Fei eff.	2.3394	1.3060	0.7459	0.3943	0.1464	0.0681
PID eff.	3.2669	0.8661	0.8898	0.5269	0.2171	0.1429
$B \to X_u \ell \nu_\ell$ BF	0.4995	0.4215	0.3507	0.3165	0.2955	0.2991
Bias corr. (stat)	0.5448	0.4884	0.4375	0.3987	0.3652	0.3539
Bias corr. (model)	9.7284	8.6597	7.2503	5.8219	4.7004	3.9025
Sys. error (total)	10.7142	8.9822	7.5167	6.0359	4.8840	4.0939
Total error	11.1360	9.0496	7.5586	6.0760	4.9103	4.1269
p_ℓ^* Cut in GeV/c	1.4	1.5	1.6	1.7	1.8	1.9
$\langle M_X^5 \rangle$ in $(\mathrm{GeV}/c1)^5$	42.5549	41.0086	38.8121	36.0142	35.6291	35.2999
Stat. error (data)	0.5452	0.6100	0.6834	0.8081	1.0206	1.3258
Stat. error (signal prob.)	0.0828	0.0071	0.0106	0.0296	0.0888	0.1766
Stat. error (total)	0.5514	0.6101	0.6835	0.8086	1.0245	1.3375
Calib. function error	1.0333	0.9615	0.8690	0.6969	0.7215	0.6895
Fei eff.	0.0099	0.0414	0.0691	0.0975	0.1463	0.2178
PID eff.	0.0972	0.0637	0.0673	0.0762	0.0895	0.1183
$B \to X_u \ell \nu_\ell$ BF	0.3015	0.3649	0.3684	0.4490	0.5789	0.8052
Bias corr. (stat)	0.3473	0.3629	0.3897	0.4350	0.5390	0.7018
Bias corr. (model)	3.0350	2.3830	1.8298	1.3269	0.8852	0.4869
Sys. error (total)	3.2404	2.6218	2.0976	1.6286	1.3997	1.3837
Total error	3.2870	2.6919	2.2062	1.8183	1.7346	1.9245

TABLE VIII: Summary of statistical and systematic uncertainties for the measurement of $\langle M_X^6 \rangle$. All values are given in $(\mathrm{GeV}/c1)^6$ if not stated otherwise. The calculation of the uncertainties is described in Section 5 5.2.

p_ℓ^* Cut in GeV/c	0.8	0.9	1.0	1.1	1.2	1.3
$\langle M_X^6 \rangle$ in $(\mathrm{GeV}/c1)^6$	151.8801	145.3258	131.9459	120.3054	108.7374	103.3617
Stat. error (data)	1.2115	1.2581	1.2752	1.3148	1.3525	1.4462
Stat. error (signal prob.)	11.9493	3.8818	2.4632	1.9239	0.6386	0.3983
Stat. error (total)	12.0106	4.0806	2.7737	2.3302	1.4956	1.5001
Calib. function error	6.3730	5.6553	4.9278	4.2983	3.6992	3.4080
Fei eff.	9.0921	4.9122	2.7203	1.4068	0.5192	0.2599
PID eff.	12.8615	2.7396	3.2193	1.8326	0.6869	0.4299
$B \to X_u \ell \nu_\ell$ BF	1.5766	1.2883	1.0012	0.8586	0.7635	0.7571
Bias corr. (stat)	1.9994	1.7482	1.5011	1.3090	1.1407	1.0690
Bias corr. (model)	32.9241	29.2623	23.9298	18.7205	14.6357	11.8590
Sys. error (total)	37.1373	30.4075	24.8584	19.4093	15.1827	12.4185
Total error	39.0312	30.6801	25.0127	19.5487	15.2562	12.5088
p_ℓ^* Cut in GeV/c	1.4	1.5	1.6	1.7	1.8	1.9
$\langle M_X^6 \rangle$ in $(\mathrm{GeV}/c1)^6$	95.6289	90.5528	83.4604	75.0624	73.7412	72.5957
Stat. error (data)	1.5273	1.6988	1.8468	2.1309	2.6788	3.4604
Stat. error (signal prob.)	0.3134	0.0532	0.0050	0.0173	0.1625	0.3796
Stat. error (total)	1.5591	1.6997	1.8468	2.1310	2.6837	3.4811
Calib. function error	3.0150	2.7442	2.3999	1.8381	1.8872	1.7875
Fei eff.	0.0746	0.0764	0.1491	0.2192	0.3380	0.5067
PID eff.	0.2739	0.1611	0.1657	0.1856	0.2133	0.2771
$B \to X_u \ell \nu_\ell$ BF	0.7394	0.9072	0.8658	1.0502	1.3508	1.8659
Bias corr. (stat)	1.0066	1.0232	1.0616	1.1438	1.4076	1.8225
Bias corr. (model)	8.9427	6.8406	5.1028	3.5697	2.3624	1.2839
Sys. error (total)	9.5238	7.4984	5.8073	4.3146	3.6205	3.4612
Total error	9.6506	7.6887	6.0939	4.8121	4.5067	4.9090